High-Throughput Route for Determining the Precise Location of an Individual Carbon Nanotube by Vapor-Phase Hydrofluoric Acid Etching

by

Michael A. Novak

Bachelor of Science, Chemistry, Saint Vincent College, 2010

Submitted to the Graduate Faculty of

the Dietrich School of Arts and Sciences in partial fulfillment

of the requirements for the degree of

Master of Science in Chemistry

University of Pittsburgh

2013

UNIVERSITY OF PITTSBURGH

Dietrich School of Arts and Sciences, Department of Chemistry

This thesis was presented

by

Michael A. Novak

It was defended on

November 5, 2013

And approved by

Dr. Haitao Liu, Assistant Professor, Department of Chemistry

Dr. Jill Millstone, Assistant Professor, Department of Chemistry

Dr. Alexander Star, Associate Professor, Department of Chemistry

Thesis Advisor: Dr. Haitao Liu, Assistant Professor, Department of Chemistry

High-Throughput Route for Determining the Precise Location of an Individual Carbon Nanotube by Vapor-Phase Hydrofluoric Acid Etching

Michael A. Novak, MS

University of Pittsburgh, 2013

Knowing the precise location of an individual carbon nanotube is of great importance in regards to studying its extraordinary properties. Until recently, this has been a complex and time consuming process. We have realized the optical visualization of an individual carbon nanotube's location via a hydrofluoric acid etching technique. This etching technique produces trenches on the Si/SiO_2 substrate which are formed by the carbon nanotube-catalyzed etching of the SiO_2 thin film. The trenches produced are visible under an optical microscope which allows for the precise location of an individual nanotube to be determined which facilitates their systematic study. Carbon nanotubes were grown by a metal-catalyzed chemical vapor deposition method. The samples were then etched and analyses of individual nanotubes were performed. The CVD grown nanotubes and etched trenches were analyzed using atomic force microscopy. Raman spectroscopy was implemented to study the effects of UV-ozone exposure on individual nanotubes within the trenches. It is shown that UV-ozone modifies the nanotubes structure by producing defects in the nanotube's graphene lattice and ultimately degrades the nanotube. The degradation of the nanotube is evident by a disappearance of the G-band in the nanotubes Raman spectrum. The hydrofluoric acid etching technique presented here provides a high-throughput route for the systematic analysis of individual carbon nanotubes which is made possible by the optical visualization of a trench which contains the nanotube of interest.

TABLE OF CONTENTS

LIST OF FIGURES

PREFACE

I would greatly like to thank my entire family and the love of my life, my girlfriend, for their advice and unconditional support. Without their advice and support, the thesis presented here would not have been possible.

1.0 INTRODUCTION

Since their discovery in 1991 by Iijima[1] carbon nanotubes (CNTs) have been a main focus of materials-based research. CNTs are model one-dimensional (1D) nanostructures and due to their superior electrical, mechanical, and optical properties they have a wide range of applications which include energy conversion, nanoelectronics, and sensing devices.[2] A more comprehensive look at their range of applications can be seen in Figure 1.

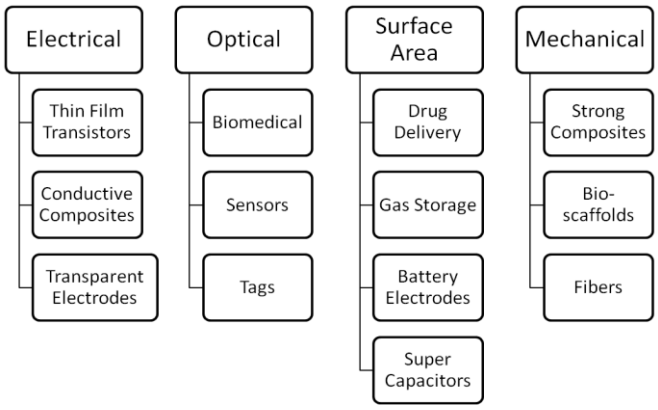

Figure 1. Applicable fields for carbon nanotubes

CNTs are unique materials which come in a variety of flavors. They can be composed of a single layer of graphene which is rolled up to form a seamless cylinder. Carbon nanotubes of this type are called single-walled carbon nanotubes (SWCNTs). They can also consist of

multiple sheets of graphene which form concentric cylinders with one inside the other. This type is referred to as multi-walled carbon nanotubes (MWCNTs). A subdivision of MWCNTs, called double-walled carbon nanotubes (DWCNTs), consists of only 2 concentric cylinders. The spacing between cylinders in MWCNTs and DWCNTs is typically on the order of 0.5 nm.[3] Not only can the number of cylinders (*e.g.* walls) differ in CNTs, but the electronic properties can also vary from tube to tube. For example, a SWCNT can be either semiconducting or metallic. MWCNTs can be composed of a mixture of semiconducting and metallic tubes. For example, a DWCNT can have 4 possible configurations (M@M, M@S, S@S, S@M) with each having different properties.[3] The electronic structure of the CNT depends on how the graphene lattice is rolled-up to form the cylinder.

The ability to study an individual CNT is of great importance in regards to their numerous application possibilities such as nanoelectronics based on an individual CNT. Raman spectroscopy is a very powerful tool for studying individual SWCNTs and provides a plethora of information about the nanotube. This information includes, but is not limited to, the nanotubes structural characteristics such as its diameter and chirality along with other information such as its electrical and phonon/vibrational properties. Raman spectroscopy also allows for analysis of the defects associated with CNTs. Defects can form in the CNTs graphene lattice during the synthesis process or they can be intentionally introduced through various types of chemical treatments, such as UV-ozone exposure.

There are other techniques available to characterize an individual CNT's structure and morphology other than Raman spectroscopy. These techniques include but are not limited to scanning electron microscopy (SEM), transmission electron spectroscopy (TEM), atomic force microscopy (AFM), and scanning tunneling microscopy (STM). Raman spectroscopy is

advantageous compared to some of the above methods, in regards to characterizing the CNTs morphology and structure, because it can be performed in ambient conditions and a CNT spectrum can be collected relatively quickly and without any sample preparation.

Determining the location of a CNT on a substrate is possible with some the above techniques but can be hindered by the use of ultra-high vacuums (UHV) or small field of view. It would be very advantageous to have the ability to determine an individual CNT's location using an optical microscope due to the fact that most labs are equipped with them, they can be used under ambient conditions, and also have a much larger field of view in comparison with the previously mentioned instrumentation. Recently, Zhang et al. reported the optical visualization of suspended individual CNTs by the chemical vapor deposition (CVD) of titanium dioxide nanoparticles onto the nanotube walls.[4] The deposition of Ag and Au has also been employed to optically visualize CNTs but in these cases the NPs primary purpose was in regards to surface-enhanced Raman spectroscopy (SERS).[5,6] The strong scattering of visible light due to the nanoparticles allows for the CNTs to be observed under an optical microscope, even with low magnification. Prior to the Zhang et al. report, an individual nanotubes location could be precisely determined by current techniques, such as e-beam lithography, which made it possible to always return to the same isolated CNT. Having the ability to always return to the same individual CNT on a substrate is of importance because it allows one to systematically study the same nanotube before and after its modification. For example, a Raman spectrum of a given individual CNT can be collected prior to any modification. The CNT can then be modified and its Raman spectrum collected from the same spot on the nanotube as the pre-modified spectrum.

The vapor-phase hydrofluoric acid (HF) etching procedure presented here allows for the location of an individual CNT to be precisely known. This etching technique is advantageous

compared to the other current techniques because of its simplicity and time-friendly approach. Ideally, a nanotube can be grown, its location precisely determined via HF vapor-phase etching, characterized by Raman spectroscopy, and modified within a day's work.

This vapor-phase HF etching procedure is based on the etching of the SiO_2 thin film that covers the Si substrate. A CNT will catalyze this etching process. Therefore, SiO_2 that is in intimate contact with the CNT will etch at a slightly faster rate compared to the SiO_2 that is not in intimate contact with the CNT. Because of this difference in etching rates, a trench around the CNT forms over time. These trenches are visible under an optical microscope due to the interference of the SiO_2 thin film.[7] The CNT-catalyzed etching of SiO_2 has been previously reported but this previous method utilized a wet-etching technique[8] compared to the vapor-phase etching method reported here. The primary advantages of the vapor-phase technique are that the CNTs remain on the substrate after the etching where as in the wet-etching process the nanotubes will be mostly washed away from the substrate which prohibits their systematic analysis. Additionally, the trenches produced via vapor-phase etching are typically deeper in comparison with trenches produces via wet-etching. Trench depth is critical for their optical detection.

Not only does this vapor-phase etching technique provide a quick route to locate and analyze a CNT, but it also has the promise for the high-throughput fabrication of nanoelectronic devices such as carbon nanotube field-effect transistors (CNFETs). Since the CNTs location can be precisely determined, metal contacts can be applied to the CNT to form an FET based on an individual nanotube. The study of nanoelectronics is of great interest to the scientific community. Over the past few decades there have been great advances in the electronics industry due to the shrinking dimensions of certain electrical components such as transistors. By shrinking the dimensions of a device, one can improve its power efficiency and speed.[9] It is expected in the

near future that current silicon technology will encounter fundamental physical limitations to size reduction. One avenue to overcome these limitations is not to change the existing technology, but to base it on new materials, such as SWCNTs. Therefore, having a high-throughput route to fabricate a CNFET based on an individual nanotube is of importance to the nanoelectronics field.

The aim of this project is to demonstrate the usefulness of the vapor-phase HF etching technique which proves as a high-throughput route for the systematic study and characterization of an individual CNT. The CNTs used in the work presented here were of the SWCNT flavor, which were grown via metal-catalyzed chemical vapor deposition (CVD). The etching process presented here was carried out on the CVD grown CNTs to produce trenches in the Si/SiO_2 substrate. The nanotubes and trenches were characterized via AFM. Following the etching procedure, the presence of a CNT within a trench was confirmed via Raman spectroscopy. Ultimately individual CNTs were modified via UV-ozone exposures and their Raman spectra analyzed. It is shown that the UV-ozone oxidation produces defects in the CNT's graphene lattice and upon increased exposure time, the CNT is almost completely degraded by the effects of UV-ozone and this is portrayed in the nanotubes Raman spectrum by the appearance of a disorder-induced D-peak and the disappearance of the tangential mode or G-peak.

2.0 CARBON NANOTUBES

2.1 WHAT IS A CARBON NANOTUBE?

Numerous types of carbon allotropes exist. They include graphite, fullerenes, graphene, and carbon nanotubes. Allotropes such as CNTs, fullerenes, and graphite are all derived from graphene. These allotropes consist of sp^2 carbons. Graphite consists of multiple layers which are held together by weak van der Waals (VDW) forces. The breaking of these VDW forces is evident in the use of graphite pencils which allows for the deposition of graphite onto paper. A single layer of graphite is known as graphene. This single layer is atomically thin and is composed of a hexagonal honeycomb lattice which consists of sp^2 carbons. SWCNTs can be considered a rolled-up version of graphene which forms a seamless cylinder where as a fullerene is more of a spherical cage of graphene.

Graphene was last of the above allotropes to be discovered (2004) while fullerenes were discovered in the 1980's and CNTs in the 1990's.[10] Fullerenes, CNTs, graphene, and graphite represent zero-dimensional (0-D), one-dimensional (1-D), two-dimensional (2-D), and three-dimensional (3-D) materials, respectively. A material that has nanoscale dimensions in all directions is 0-D. A material with nanoscale dimensions in all directions but one is a 1-D material. As previously mentioned, a CNT is a 1-D material due to its nanoscale dimensions except for its length, which can be on the order of millimeters or centimeters. A 2-D material has

nanoscale dimensions only in one direction, such as graphene or a thin film. For example, a sheet of graphene may be 1 cm^2 but only an atom thick. A 3-D material such as diamond or graphite does not possess any nanoscale dimensions and can be considered as bulk materials.

2.2 GEOMETRIC STRUCTURE OF SWCNTS

Single-walled carbon nanotubes can be considered as model 1-D structures. Their diameter is typically on the order of 1-2 nm but their length can be on the order of millimeters or even centimeters. A SWCNT can be looked at as a single layer of graphene which is rolled up to form a seamless cylinder. Depending on how the graphene sheet is rolled up, 3 types of CNTs can be formed. They are designated as armchair, zigzag, or chiral as shown in Figure 2.1.[11] Furthermore, a SWCNT can be characterized by its chiral vector C_h. This chiral vector is often described by a pair of indices (n,m) which is referred to as chiral indices. The chiral indices indicate the number of graphene unit cell vectors, na_1 and ma_2, in the hexagonal honeycomb lattice contained in C_h. This is shown in equation 1.[12] This chiral vector forms an angle (θ) with the zigzag direction, which is known as the chiral angle. For a zigzag SWCNT $\theta = 0^\circ$, for an armchair SWCNT $\theta = 30^\circ$, and for a chiral SWCNT $0 < \theta < 30^\circ$ as show in Figure 2.

$$C_h = na_1 + ma_2 \quad (1)$$

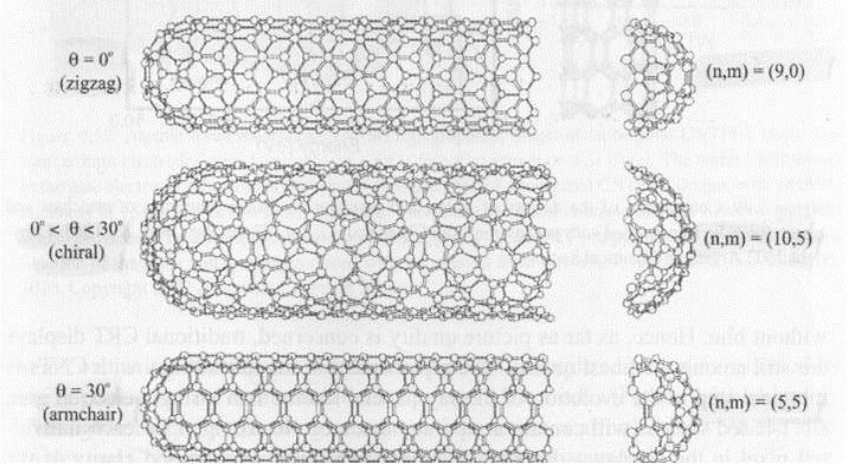

Figure 2. Illustration of the three types of CNTs showing the relation between the chiral angle and the type of nanotube. Also note the chiral indices on the right side of the illustration. Reprinted from Dresselhaus, M. S.; Dresselhaus, G.; Eklund, P. C. *Science of Fullerenes and Carbon Nanotubes*, Copyright 1996, with permission from Elsevier. [11]

The schematic shown in Figure 3 is a visual representation showing various ways the 2-D graphene lattice can be rolled- up to form a 1-D SWCNT. For example, in the top schematic of Figure 3, if point A is rolled to point A' a CNT with unique chiral indices is formed. Here, points A and A' represent the initial and terminal points of the chiral vector, respectively. The initial point A would be at (0,0) and terminal point A' would be at (n,m). This schematic could be extended to form larger diameter SWCNTs.

From the schematic shown in 3 (bottom), it can be seen that when n = m, the SWCNT will be of the armchair type. When m = 0, the SWCNT is of the zigzag type. For all other values of (n,m), the SWCNT is considered chiral. Also note that the various (n,m) indices shown in Figure 3 are labeled as metallic or semiconducting. The electronic properties of SWCNTs will be discussed in more detail in the following section.

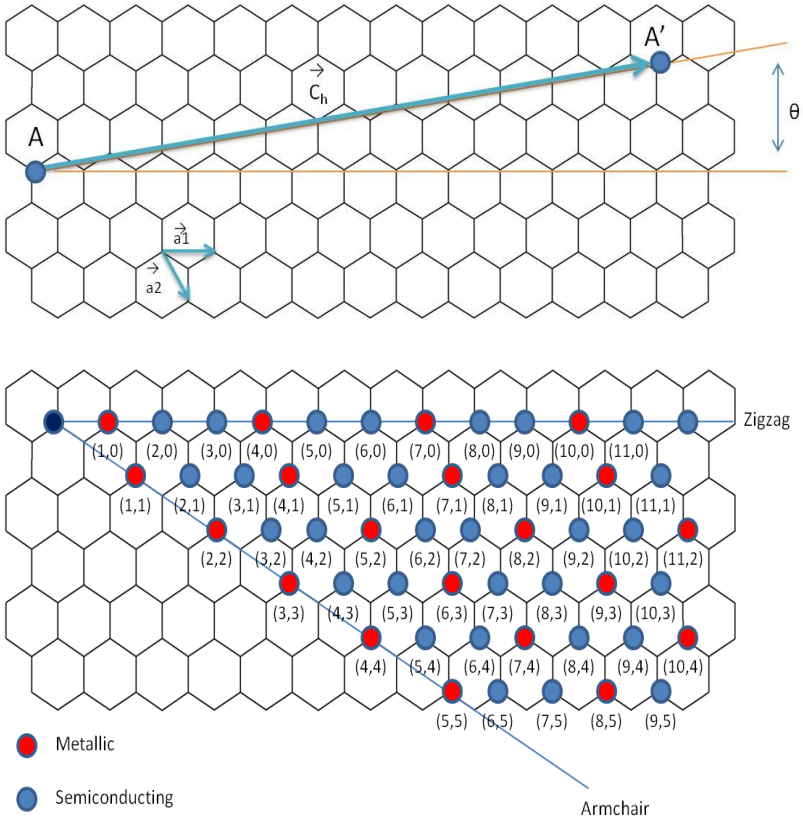

Figure 3. Schematics showing the various ways a SWCNTs 2-D graphene lattice can be rolled-up to form a 1-D nanotube. Each, the chiral vector (Ch) and chiral angle (θ), is indicated along with the graphene unit cell vectors a1 and a2 (top). The Chiral indices for various types of SWCNTs. Note that n = m and m = 0 for armchair and zigzag SWCNTs, respectively. Armchair nanotubes will always have metallic character as shown above (bottom).

Knowing the (n,m) indices allow one to determine various characteristics of that given SWCNT. For example, one can calculate the nanotube diameter (d_t), the chiral angle (θ), and the

length of C_h (L). The chiral indices can also be used to study the electronic structure of CNTs which is the focus of the following section.

2.3 ELECTRONIC STRUCTURE OF SWCNTS

The electronic structure of SWCNTs can vary from semiconducting to metallic. The electronic differences between SWCNTs arise from how the graphene honeycomb lattice is rolled up. Therefore, the electronic structure is very closely related to a SWCNT's chiral indices (see Figure 2.2). An armchair SWCNT (n = m) will always be metallic where as zigzag (m = 0) and chiral SWCNTs can be either metallic or semiconducting. If one was equipped with a SWCNTs chiral indices it is still possible to determine whether a SWCNT is metallic or semiconducting without the use of an illustration as shown in Figure 3. For example, SWCNTs for which |n-m| = 3q are metallic and SWCNTs for which |n-m| = 3q +/- 1 are semiconducting. For each case "q" is an integer.[13]

Since a SWCNT is derived from a single layer of graphene, one can gain a deeper explanation of the electronic structure of SWCNTs by analyzing its parent structure (*e.g.* graphene) and then applying it to CNTs. This is explained by concepts such as the density of states (DOS), Brillouin zones, cutting lines, and the zone-folding scheme.

In solids, the electronic states have a continuous range of energies. However, this is not the case for molecules and atoms, which have discrete energy states.[14] An illustration of this can be seen in Figure 4.[14] As you move from a bulk material (3-D) to a 0-D material the DOS become quantized. A CNT would resemble the DOS of a quantum wire. The CNT's DOS are

characterized by very sharp peaks known as van Hove singularities (VHS) as shown in Figure 4. These singularities define narrow energy ranges where the DOS becomes very large.

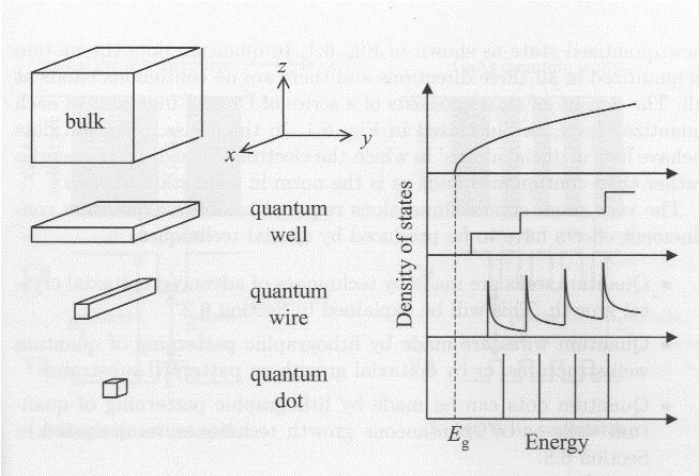

Figure 4 . Illustration showing the density of states (DOS) of bulk, 2-D (quantum well), 1-D (quantum wire), and 0-D (quantum dot) materials. E_g represents the band gap of the material. Reprinted from Fox, Mark. *Optical Properties of Solids*, Copyright 2010, with permission from Oxford University Press.[14]

The first Brillouin zone of graphene is defined using a reciprocal lattice and consists of a single hexagon. The first Brillouin zone of graphene can be considered to be a single hexagon in Figure 5, which includes the high-symmetry points of Γ, M, K, and K'. The first Brillouin zone of a CNT is 1-D due to the fact that the CNT itself is 1-D. The 1-D Brillouin zone of the CNT can be expanded onto the reciprocal space of 2-D graphene in the form of cutting lines.[15] This process is known as "zone-folding". In other words, the zone-folding scheme allows for the mapping of the reciprocal space of a single layer of graphene onto the reciprocal space of a CNT

via construction of the cutting lines which is based on the geometric structure of the nanotube itself.[15] Cutting lines are represented in Figure 5 as the series of parallel equidistant lines.

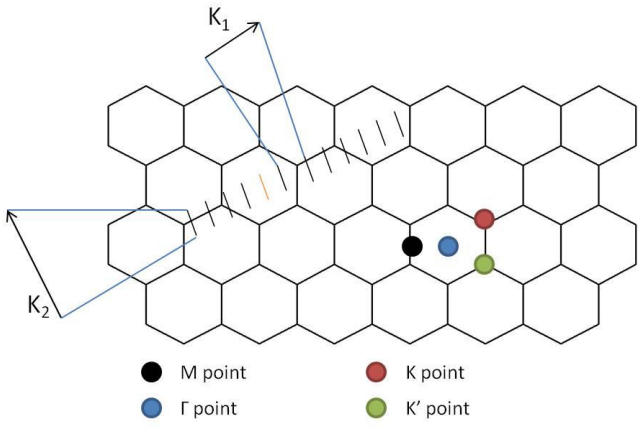

Figure 5. Illustration showing the reciprocal space of a single layer of graphene. The high-symmetry points are labeled as Γ, M, K, and K'. K_1 and K_2 represent the reciprocal space vectors of the nanotube. The series of parallel equidistant lines represent the cutting lines for a nanotube.

It is shown in Figure 5 that the vectors K_1 and K_2 are orthogonal to each other. These vectors represent the reciprocal space vectors of the CNT and the cutting lines produced from these vectors are quantized in the K_1 direction and continuous in the K_2 direction. There is a certain length and spacing related to these cutting lines. The number of cutting lines is determined by the cutting line index μ which is an integer and varies from 1-N/2 to N/2 where "N" represents the number of hexagons in the CNT unit cell and is always an even number.[15] As an example, for a (4,2) CNT, N = 28, hence there are 28 cutting lines. The cutting line at the high symmetry point Γ (orange cutting line in Figure 2.4) would be "0" and the cutting line directly to its right and left would be "1" and "-1", respectively. For a (4,2) CNT, the cutting

lines would range from -13 to 14 for a total of 28. The length/orientation and the spacing of the cutting lines in are given by the vectors K_2 and K_1, respectively. The distance between two neighboring cutting lines is related to d_t by the relationship $|K_1| = 2/d_t$.[12]

So, what do the DOS, Brillouin zones, cutting lines, and zone-folding have to do with the electronic structure of CNTs? Well, the position of the cutting lines in the Brillouin zone of graphene, relative to the high-symmetry points, dictates whether that given CNT is semiconducting or metallic. If cutting lines pass through the high-symmetry points K and K', the CNT is metallic. If cutting lines do not pass through these points, the CNT is semiconducting.[15] The reason that the K and K' points are of interest is because this is where the valence and conduction bands touch which leads to the "zero band-gap" semiconductor characteristics of graphene. This is illustrated in Figure 6,[16] which is a 3-D map of graphene's hexagonal first Brillouin zone. The π and π* bands represent the valence and conduction bands, respectively. The high-symmetry points M, K, and K' are labeled. The hexagonal black line indicates the first Brillouin zone of graphene and the other high-symmetry point Γ would be located at the center of the hexagon. It can be seen that the valence and conduction bands touch at both the K and K' points.

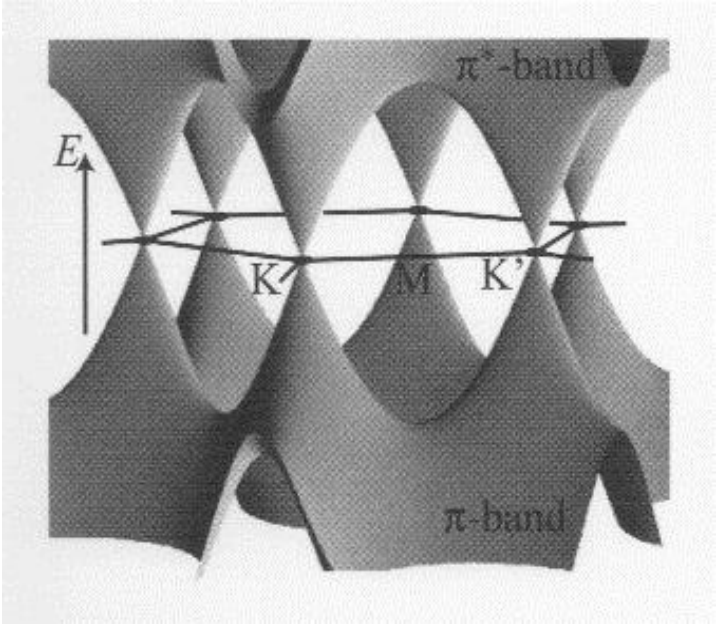

Figure 6. Three-dimension image showing the valence (π) and conduction (π*) bands of graphene. These bands touch at the high-symmetry points K and K'. The black hexagonal line indicates the first Brillouin zone of graphene. Reprinted from Ihn, Thomas. *Semiconductor Nanostructures*, Copyright 2010, with permission from Oxford University Press.[16]

The chiral indices (n,m) are unique to a certain type of CNT. These indices define how the 2-D graphene lattice is rolled up to form a 1-D CNT. Because the (n,m) indices are unique to a certain CNT, each (n,m) CNT will have its own distinct electronic structure and therefore its own unique DOS plot.

2.4 CARBON NANOTUBE SYNTHESIS METHODS

There are numerous ways to synthesize CNTs. The three primary ways are laser ablation, arc discharge, and CVD with the latter presently being the most popular.[17] Each of these techniques have advantages and disadvantages which are discussed below.

Arc discharge and laser ablation are two similar techniques used to produce CNTs. Arc discharge techniques use a pair of high quality graphite electrodes.[18] The carbon atoms of the electrodes are evaporated by a helium plasma which is formed by passing a high current between the graphite electrodes. This method is a high temperature method (> 1700˚C) and is typically performed at non-ambient pressures. This type of synthesis is sensitive to the atmospheric conditions in which it is performed and mostly produces CNTs with fewer structural defects when compared to other methods.[17] A disadvantage of the arc discharge method is that it usually produces a mixture of materials and typically requires a separation step to remove the CNTs from the soot and metal catalysts.[19]

In the laser ablation technique a laser is focused onto a graphite target (or graphite-metal composite) which is placed in a furnace and heated to high temperatures (≈1200˚C). The laser vaporizes the target which results in CNT formation. This method favors the growth of SWCNTs rather than MWCNTs. A primary disadvantage of this method is that it produces only a small carbon deposit.[18]

So, why is CVD currently the synthesis method of choice? First, CVD is a popular method because it has a high production yield, can be easily scaled-up, and is cheap.[17] A second advantage of CVD is that it can be carried out under ambient pressure and at lower temperatures than arc discharge or laser ablation. Thirdly, CVD allows for better control of the nanotube

alignment, density, and orientation as compared to laser ablation or arc discharge which typically produces jungle-gym arrays of nanotubes which can be very dense.[19] A jungle-gym structure can be looked at as a highly entangled array of CNTs. Lastly, using the CVD method allows for the use of various types of substrates on which the nanotubes can be grown. Commonly used substrates are silicon/silicon dioxide and quartz.

The type of CVD employed in the project presented here is known as catalytic chemical vapor deposition (CCVD). In general, CVD is a process which produces a solid material (nanotube, graphene, thin film,) by reacting a volatile compound of the parent material (*e.g.* the carbon source for CNT growth).[20] CCVD was the method used in the project presented here, therefore it is the primary focus of this section.

Typically, CCVD processes involve the thermal decomposition of a carbon source in the presence of a metal catalyst, hence it is known as catalytic-CVD. Typically the carbon source is a hydrocarbon such as ethanol or methane. The carbon feedstock material can be in the liquid or gas phase. If the carbon feedstock is in the liquid phase, it is typically introduced into the CVD chamber by passing a carrier gas, such as argon, through the liquid.

Various types of catalysts can be employed during CCVD growth. The most commonly used catalysts are metals such as iron, cobalt, and nickel. The reason that these are popular metal catalysts is because at high temperatures, carbon has a high solubility and a high diffusion rate in them.[17] Solid organometallocenes (ferrocene, nickelocene) can also be used as a catalyst because they can produce metal nanoparticles in-situ. These nanoparticles then catalyze the decomposition of the carbon source.[21] Regardless of the type of catalyst used during CVD it is desirable to have the carbon source decompose on only the catalyst nanoparticle and not in the gas environment above the growth substrate.

The catalyst plays a very important role in the CCVD process. First, the nanometer sized particles allow for the decomposition of the carbon source at a lower temperature than the spontaneous decomposition temperature.[17] Secondly, they dictate the diameter of the CNT. For example, the larger the metal nanoparticle the larger the CNT diameter.

The actual nanotube growth mechanism is under debate. A widely accepted mechanism involves the decomposition of the carbon source (*e.g.* hydrocarbon) on the metal nanoparticle. The hydrocarbon decomposition produces carbon and hydrogen. While the hydrogen is carried away by the gas flow in the reaction chamber, the carbon dissolves into the metal. Once the carbon reaches its solubility limit in the metal, it precipitates out as a cylindrical nanotube as reported by Raty et al.[22] As the carbon atoms precipitate out of the nanoparticle, they diffuse across the surface and form a graphene cap and as new carbon atoms are added, the cap is pushed away from the nanoparticle and a tube is created.

There are two widely accepted models which are the base-growth and tip-growth models. An illustration of these growth mechanisms can be seen in Figure 7 where the green arrows represent the incoming carbon source and the Fe catalyst particles are indicated. With the base-growth mechanism, the catalyst particle remains stationary on the substrate as the nanotube emerges. In contrast to the base-growth model is the tip-growth model. Here, the catalyst particle remains at the tip of the nanotube during growth and is not stationary.

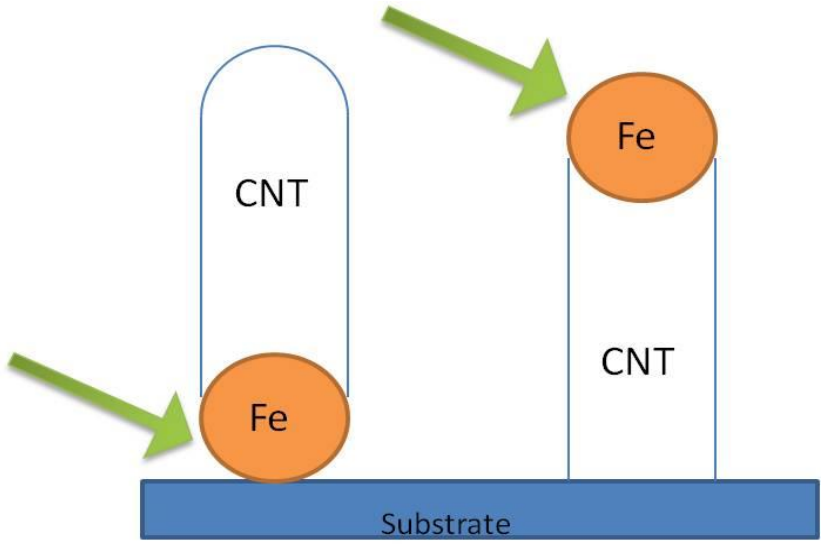

Figure 7. Illustration of two mechanisms for CNT growth. (a) Base-growth model and (b) tip-growth model. The green arrows represent the incoming carbon source and the Fe catalyst particles are labeled.

2.5 CARBON NANOTUBE CHARACTERIZATION METHODS

There are numerous methods used to characterize CNTs. A few of these methods include Raman spectroscopy, AFM, scanning tunneling microscopy (STM), and electron microscopy. This section will focus on AFM and Raman spectroscopy due to the fact that these were the two primary methods used for CNT characterization in the project presented here.

2.5.1 Atomic Force Microscopy

Atomic force microscopy is a subdivision of scanning probe microscopy (SPM). There are two major classes of SPM, which are STM and AFM. Both of these techniques provide a topological image of the sample surface. An advantage of SPM and AFM is that they can be carried out in ambient temperatures and pressures. Although, they can be performed in an ultra-high vacuum chamber if there is a need to prevent contamination.[23] The primary difference between these two techniques is that in STM, the tunneling current between the tip and sample is analyzed whereas in AFM, the force between the tip and sample is analyzed. This force can be explained by Hooke's law.[24] Since a current is analyzed during STM, the sample must be conducting where this is not the case in AFM. Both AFM and STM possess atomic resolution.

AFM is a very powerful tool when studying nanomaterials. During AFM, a probe is rastered across the sample surface ultimately providing a topological image of the sample surface. A typical AFM illustration is shown in Figure 8. Briefly, a laser is reflected off the top of the AFM probe. This reflection is then collected by a photodiode detector. The deflection off of the probe changes as the tip encounters a material, such as a CNT, as it is rastering across the sample surface. These very small changes in deflection are then processed into a topographical map of the sample surface.

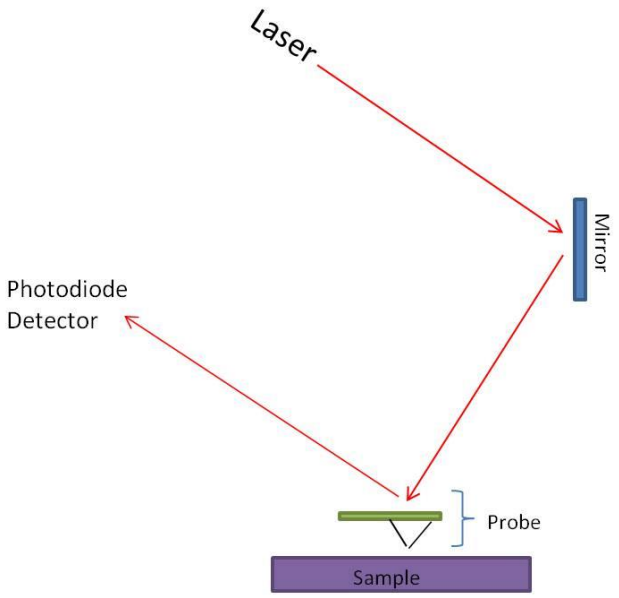

Figure 8. Illustration showing the mechanism by which an AFM instrument maps the topography of a sample.

Three typical AFM modes are contact, non-contact, and tapping mode. When using contact mode, a piezoelectric response in the AFM cantilever raises or lowers the probe to maintain a constant force between the probe and sample. Usually contact mode is best suited for hard samples. During non-contact mode, the AFM tip is kept above the sample surface, typically on the order of a few Angstroms. Here, the weak attractive van der Waal forces between the oscillating probe and sample surface are monitored. This method is best for soft surfaces. Tapping mode also involves an oscillating probe. This oscillation is constant when the probe is not in contact with the sample surface. The tip is moved downwards until it reaches the surface. As the tip rasters across the surface, it encounters changes in the surface elevation and this changes the amplitude of oscillation. This change is detected and ultimately provides a topological image of the surface.[23] Tapping mode can be used on hard or soft samples.

As previously mentioned, the resolution of AFM is on the atomic scale. This resolution is dependent on the size of the tip.[24] The smaller the radius of curvature, the better the resolution. Currently, there are efforts being made to produce AFM probes that implement the use of a CNT as the probe tip.[25] It should also be noted that the resolution decrease as the tip is moved farther from the sample surface. Hence, non-contact mode images are usually not as highly resolved as the other AFM modes.

2.5.2 Raman Spectroscopy

Raman spectroscopy is another very powerful tool for analyzing CNTs. It can provide a plethora of information including, but not limited to, the CNTs chirality, diameter, electrical characterization (metallic vs. semiconducting), phonon and electron properties, and defect density.[26] Not only does the abundance of information provided by Raman spectroscopy make it a popular characterization technique, but it also has advantages over other characterization techniques in that Raman can be performed under ambient pressure and temperature, a spectrum can be collected in a relatively short time period, and there is typically little or no sample preparation required. It should be noted that since Raman spectroscopy implements the use of a laser, sample degradation is possible if the sample is sensitive to the laser. This can usually be avoided by adjusting the laser power before collection of the spectrum.

Raman spectroscopy is a form of vibrational spectroscopy which is based on the scattering of light. Incident light (monochromatic), typically from a laser of frequency ν_o impinges on the sample. The sample then scatters this incident light in two ways. Most of the light is scattered through a phenomenon called Rayleigh scattering. This scattered light has the same frequency as the incident light. This is an elastic collision between the sample and the

incoming photons. A very small amount of light is scattered at a different frequency (ν_i) than the incident light. This can be thought of as inelastic collisions between the sample and the incoming photons. Scattering of this type is called Raman scattering. The phenomenon of Raman scattering was discovered by Chandrasekhara Raman in 1928.[27] A schematic of a typical Raman setup can be seen in Figure 9. The incident light is scattered off of the sample via Rayleigh or Raman scattering. From there, the scattered light passes through a series of filters, mirrors, and a grating. This grating disperses the light onto a charged coupled device (CCD). The final result is the Raman spectrum of the sample. A typical spectrum is a plot of Raman intensity vs. Raman shift.

Raman Scattered light from the sample can have a frequency greater than the incident light ($\nu_i > \nu_o$) or less than the incident light ($\nu_i < \nu_o$). The amount of scattered light with a frequency lower than the incident light ($\nu_i < \nu_o$) is much greater than the amount of scattered light with a frequency higher than the incident light ($\nu_i > \nu_o$) which are known as stokes and anti-stokes scattering, respectively.[28] Because of this unequal scattering of the incident light, stokes peaks are more intense than anti-stokes peaks in the Raman spectrum.

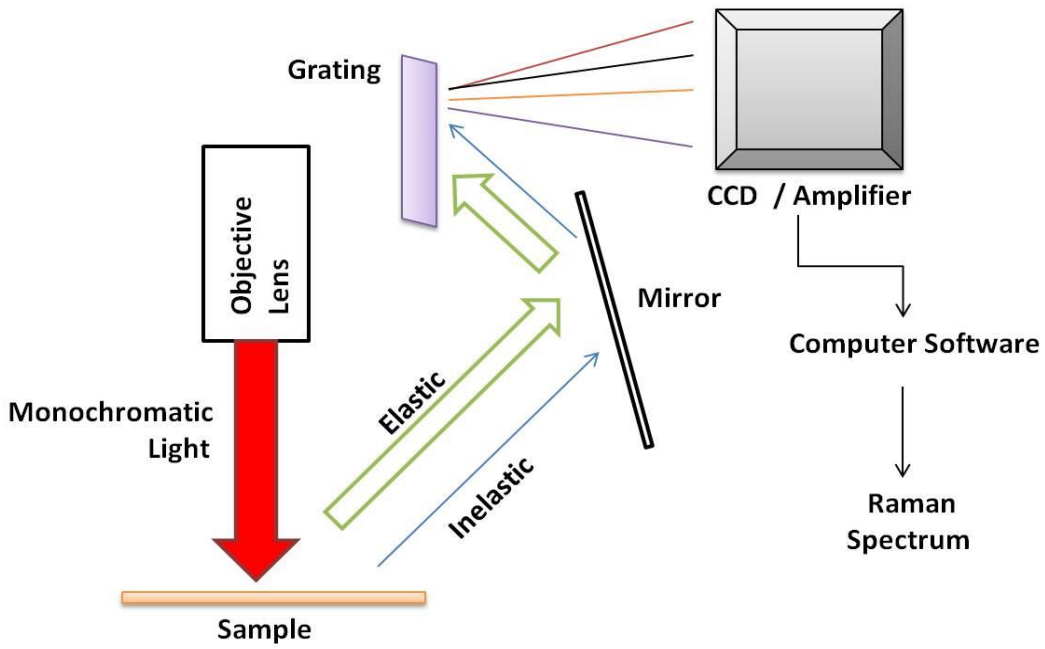

Figure 9. A schematic of a typical Raman setup. Note the widths of the arrows for elastic and inelastic scattered light. This corresponds to the amount of each type of scattered light.

The anti-stokes scattering starts from an excited vibrational state and there are typically less molecules in this excited state as compared to the ground state. Hence, the anti-stokes Raman peaks are less intense than stokes peaks. These Raman scattered peaks are very interesting because the change in energy of the scattered photons corresponds to the quantized energy levels of the sample.[27] This is shown in Equation 2.

$$\Delta E \text{ (photon)} = \Delta E \text{ (energy level)} \qquad (2)$$

Briefly, the concept of resonant Raman spectroscopy should be noted. This phenomenon is what allows for the collection of a Raman spectrum from an individual CNT. It is quite

extraordinary that a Raman signal can be collected from a material that has a diameter of 1 nm, given the diameter of a typical laser spot is on the order of 1 μm. This resonance effect is related to the electronic transition between the sharp VHSs in the valence and conduction bands of the nanotube.[29] When there is resonance between these electronic transitions (E_{ii}) and the incident/scattered photons, the Raman signal becomes greatly enhanced due to the strong coupling which occurs between phonons and electrons of the CNT.[13] This strong enhancement in the Raman signal allows for the analysis of each feature in an individual CNTs Raman spectrum that is normally observed from CNT bundles.

As previously stated, the Raman spectrum from an individual CNT is rich in information about that given CNT. A typical Raman spectrum from a SWCNT is shown in Figure 10.[29] The RBM, D, G, and G' bands are the usual peaks used when analyzing the CNT. The very small peaks to the higher frequency side of the G-peak are known as combination modes or 2nd order peaks. These modes do provide some information about the nanotubes phonon structure but were not analyzed in the project presented here. The peaks marked with an asterisk arise from the Si/SiO_2 substrate.

The radial breathing mode (RBM) is unique to CNTs. It arises from the atomic vibrations of the carbon atoms in the radial direction. The RBM feature appears for SWCNTs with a diameter between 1-2 nm in the 120 and 250 cm^{-1} range. This feature is very dependent on the diameter of the CNT, which makes sense because it corresponds to the radial motion of the carbon atoms. With a larger CNT diameter more carbon atoms are involved in the radial breathing process. Typically the RBM mode is too weak to be observed for larger diameter tubes.[30]

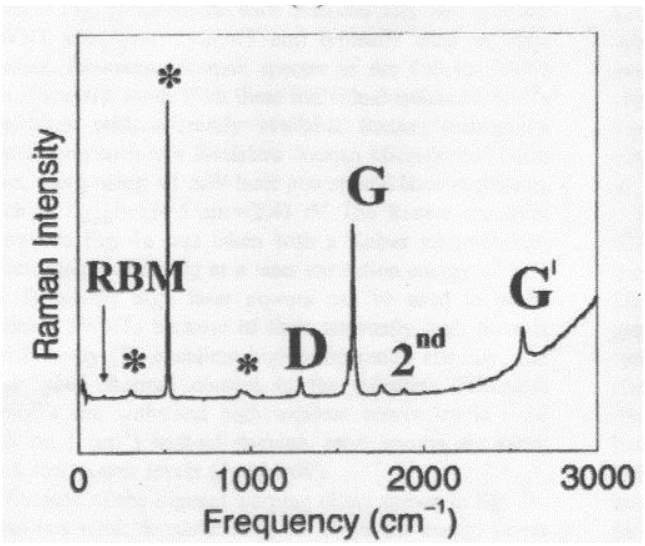

Figure 10. : Raman spectrum collected from an individual SWCNT. The bands arising from the CNT include the RBM, D, G, G', and 2nd order peaks. The peaks marked with an asterisk are from the Si/SiO_2 substrate. Reprinted from Carbon, 40, Dresselhaus, M.S.; Dresselhaus, G.; Jorio, A.; Filho, A.G. Souza.; Saito, R. *Raman spectroscopy on isolated single wall carbon nanotubes*, 2043-2061, copyright 2002, with permission from Elsevier.[29]

SWCNTs with different diameters will have different RBM spectra. The relationship between the RBM frequency (ω) and the diameter is shown in Equation 3.[31] Here, d_t is the nanotube diameter and α is a parameter determined experimentally and is 248cm^{-1} for individual CNTs on a Si/SiO_2 substrate.

$$\omega_{RBM} = \alpha / d_t \qquad (3)$$

Once the nanotube diameter is calculated, it is then possible to determine the chiral indices (n,m) of the given nanotube. It is helpful to have a plot such as the one shown in Figure 11.[32] This Figure is known as a Kataura plot.

Once the diameter of a SWCNT is determined, a plot of this type can be used to determine (n,m). Each point in the plot represents an optically allowed transition for a specific (n,m) tube.[26] If the diameter of a nanotube is 1.25 nm and the laser used has an energy of 1.96 eV, one can determine where these lines intersect on the Kataura plot and that intersection will correspond to specific (n,m) indices. It should be noted that there is a small resonance window in regards to E_{ii} and the laser used. This window is around ±0.1 eV.[13] thus the laser energy must typically be within a ±0.1 eV range of the E_{ii} energy to obtain a Raman signal.

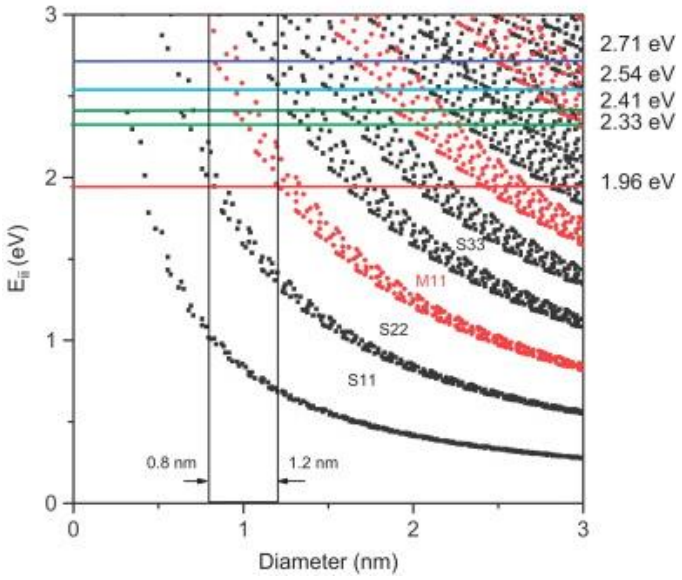

Figure 11. Kataura plot used for determination of the chiral indices for a CNT. The different colored arms of the plot correspond to semiconducting (black) or metallic (red) CNTs. Each arm is labeled as Sii or Mii where ii and S/M correspond to the VHSs relative to the Fermi level and semiconducting/metallic, respectively. Some common laser energies are indicated on the right side of the Figure. Each dot in the plot represents specific (n,m) indices. Reprinted from Physica E, 40, Liu, Jie; Dossot, Manuel; Olevik, David; Mamane, Victor; Vigolo, Brigitte; Abrahamsson, David; Jonsson, Henrik; Fort, Yves; Humbert, Bernard, Soldatov, Alexander V.; McRae, Edward *Preferential functionalization of carbon nanotubes probed by Raman spectroscopy*, 2343-2346, copyright 2008, with permission from Elsevier.[32]

Another Raman band used in CNT analysis is known as the tangential or G-band. This band is observable for all sp^2 carbon materials[29] and does slightly vary from material to material. For SWCNTs, the G-band typically is a multi-peak feature in contrast with MWCNTs and highly ordered pyrolytic graphite (HOPG) which typically consist of a single peak.[30] The splitting and shape of the G-band is very important when analyzing a CNTs Raman spectrum. First, the splitting of the G-band can provide insight into the nanotubes diameter. The splitting is labeled as G^+ (higher frequency ω_G^+) and G^- (lower frequency ω_G^-). This splitting is due to the 1-D nature of the nanotube. The G^+ and G^- portions of the G-band arise from the vibrations along the nanotube axis and nanotube circumference, respectively. Since G^+ associated with vibrations along the CNT axis, it is independent of the tube diameter while G^- is dependent on diameter.[33] This dependency of G^- on the diameter makes sense since it is related to vibrations around the nanotubes circumference.

This peak-splitting is of interest because it can be used to calculate d_t via Equation 4 if no RBM mode is observed.[29] Using this equation, ℓ=47.7 cm^{-1} nm^2 for semiconducting tubes and ℓ=79.5 cm^{-1} nm^2 for metallic tubes.

$$\omega_G^- = \omega_G^+ - \ell/d_t^2 \qquad (4)$$

As previously stated, a second important aspect of the G-band in regards to studying a CNT is its line shape. The G^- line shape is very broad for metallic tubes in comparison with that

of semiconducting tubes. Metallic CNTs possess free electrons and this broadening is related to the presence of these electrons.[30] For each type of CNT (metallic and semiconducting) the G^+ portion has a Lorentzian line shape. The G^- portion differs from a Lorentzian to a Breit-Wigner-Fano line shape for semiconducting and metallic tubes, respectively.[29]

Another Raman band of interest in a CNT spectrum is the disorder or D-band. This band is typically found in the 1250-1440 cm^{-1} range and is indicative of defects in the graphene lattice.[30] A CNT that is relatively free of defects should not show a D-band in its Raman spectrum. This defect can be a vacancy in the honeycomb lattice which produces 7 or 5 carbon-atom rings rather than a 6 carbon-atom ring (hexagon). Another type of defect is related to adding functional groups to the CNT sidewall. This creates sp^3 carbons. Defects ultimately break the symmetry of the graphene sheet which comprises the CNT.[29] This breaking of the symmetry is what gives rise to the D-band. Defects can occur in the CNT during the synthesis procedure or they can be intentionally introduced into the nanotubes graphene lattice. It should be noted that the intensity ratio I_D / I_G (D:G ratio) can be used to calculate the defect density of a CNT.[34]

3.0 EXPERIMENTAL

3.1 MATERIALS

The Si/SiO_2 wafers used in this project were purchased from University Wafer. The Si substrate supported a thermally-grown SiO_2 thin film (≈300 nm thick). The $FeCl_3$ used to prepare the catalyst solution was purchased from Fisher Scientific. Ethanol (anhydrous) was purchased from Pharco-AAPER. Sulfuric acid was purchased from Spectrum Chemical Mfg. Corp. Hydrogen peroxide (30% wt. soln in water), hydrofluoric acid (≥48%), and methanol (≥99.8%) were purchased from Sigma-Aldrich.

3.2 INSTRUMENTATION

The CVD-grown nanotubes and trenches were characterized via AFM using the tapping mode (VEECO equipped with Nanoscope IIIa software). The nanotubes themselves were also characterized by Raman spectroscopy (HORIBA XploRA micro-Raman instrument equipped with an Olympus BX51 confocal microscope and LabSpec5 software). For collection of the Raman spectra, the approximate size of the laser spot was ≈1 μm using a 100x objective. This was calculated by the relationship $1.22\lambda / NA$ where λ and NA represent the wavelength of the laser and the numerical aperture of the objective, respectively. The laser power was typically

kept at ≈3 mW to avoid heating effects. The thickness of the SiO_2 thin film (pre and post etching) was measured using a J.A. Woollam Co. alpha-spectroscopic ellipsometer with CompleteEASE software. Optical images of the wafers/trenches were collected using an Olympus BH-2 microscope (50x objective) with Motic Images Plus 2.0 software. A NovaScan Digital-Pro UV-ozone setup was used to modify the CNTs. Ozone was generated in an O_2 atmosphere using a pressurized mercury lamp. The Hg lamp used 185 nm light to produce ozone and no filter was used during CNT oxidation.

3.3 WAFER PREPARATION

Prior to CVD synthesis of the nanotubes, the Si/SiO_2 wafers were cleaned with piranha solution. *Warning: Piranha solution presents an explosive danger and is a strong oxidant. All work with piranha solution should be done in a fume hood. Handle with extreme care.* This solution was comprised of a 3:1 ratio of H_2SO_4 : H_2O_2. The piranha solution containing the wafers was heated on a hot plate to ≈80°C and was left for 30 minutes. The wafers were then rinsed with DI water and dried with a stream of N_2.

3.4 CATALYST PREPARATION / APPLICATION

A 0.1M $FeCl_3$ catalyst solution was prepared for the Fe-catalyzed CVD growth of the CNTs. The catalyst solution was manually applied to one end of the substrate. Typically 4 samples were

placed in the quartz furnace tube per growth process. The catalyst end of the substrate was placed towards the gas flow entrance.

3.5 CHEMICAL VAPOR DEPOSITION

A hot-walled CVD reactor was used for the synthesis of CNTs. After the samples were placed into the 1" quartz tube, the CVD system was purged with Ar and H_2 which had flow rates of 250 and 26 standard cubic cm (sccm), respectively. The CVD furnace was then allowed to heat to 900°C and the samples were allowed to calcine at this temperature for 30 minutes. The Ar/H_2 gas mixture was then routed through a bubbler containing the carbon stock ethanol (EtOH), and CNT growth was initiated. Throughout a typical CVD process, three growth cycles were performed. The first cycle was allowed to proceed for 15 minutes and the second and third cycles each for 10 minutes. Between each growth cycle, the gas mixture was re-routed to bypass the carbon stock so it would directly enter into the growth chamber. Each period between growth cycles continued for 3 minutes. This multiple-cycle growth method was adapted from the Liu group at Duke University.[35] After the final growth cycle the gas mixture was allowed to flush out any excess EtOH from the chamber prior to opening the furnace to cool. The cooling took place with the gas mixture still flowing. The presence of CNTs was then confirmed via AFM.

3.6 HYDROFLUORIC ACID VAPOR-PHASE ETCHING

For the etching of the CNT samples, a home-made etching chamber (≈300 cm^3) was constructed. An illustration of the etching chamber can be seen in Figure 12. This chamber contained a heating block, which the samples were placed on, and heating tape. The temperature of the heating block was controlled by the ΩE Omega bench top controller. The two reagents used were HF and Methanol (MeOH). *Warning: HF acid is highly corrosive and poisonous. It can penetrate through tissue and bones and should only be used in a fume hood. Symptoms of HF exposure may not be immediately evident. Handle with extreme care.* These reagents were kept in small containers which were ultimately placed into the chamber to initiate etching. Reagents that had been used for ≈140 etching minutes were replaced with fresh reagents. Only one sample was etched at a time and was also allowed to pre-heat to 70-100°C before etching was initiated. A sample was exposed to the etching vapors for 30-70 minutes. During this exposure the chamber was sealed. The presence of the trenches formed by CNT-catalyzed etching was then confirmed via AFM and optical microscopy. The presence of a CNT within a trench was confirmed via Raman spectroscopy.

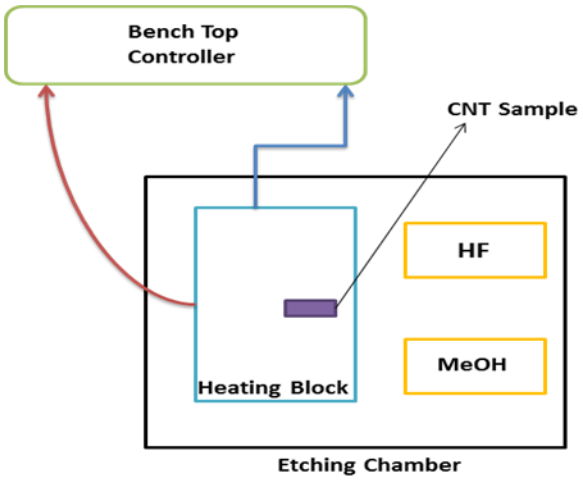

Figure 12. : Schematic of the home-made etching chamber which is approximately 300 cm3. The red arrow indicates the thermocouple connection to the bench top controller and the blue arrow indicates the heating tape connection.

3.7 UV-OZONE OXIDATION OF CARBON NANOTUBES

Etched samples containing nanotubes were subsequently modified via UV-O_3 oxidation. This oxidation was performed under ambient temperature and pressure. Each sample was placed ≈5 cm away from the pressurized Hg lamp and only one sample was oxidized at a time. Prior to turning on the lamp, the chamber was purged with O_2 for ≈4 min before the exposure time was set. Samples were treated for varying amounts of time. Raman spectra from the same individual CNT were collected pre and post UV-O_3 exposure.

4.0 RESULTS AND DISCUSSION

4.1 CVD SYNTHESIS OF CARBON NANOTUBES

Carbon nanotubes used in this project were synthesized via a Fe-catalyzed CVD procedure and ethanol (EtOH) was used as the carbon stock. Initially, a single-cycle growth method was employed to grow the CNTs. This method was adopted from Zheng et al.[36] and has the capability to produce ultra-long CNTs, sometimes on the order of centimeters. Theoretically, the CNTs can grow as long as the substrate. This single-cycle growth did produce CNTs but with a very low density. Therefore, the CVD procedure was modified to incorporate a multiple-cycle growth method which was adopted from Zhou et al.[35] This multiple-cycle procedure was incorporated in hopes that it would increase the CNT density. An increased density helps facilitate the characterization of CNTs via AFM. With a higher density, less time has to be spent searching for CNTs. It should be noted that a very high density of CNTs is not ideal either. If the density is too high, it becomes difficult to distinguish between different CNTs. Also, in the project presented here, a very high density would inhibit the study of an individual CNT. For example, it would be difficult to analyze an individual CNT if the laser spot (Raman spectroscopy) encompassed multiple nanotubes that gave a Raman signal.

With the one-cycle growth method, the CNT growth was initiated by routing the gas flow into the bubbler containing the carbon source. The growth was allowed to proceed without

interruption. Therefore, this is only a one-growth cycle. In contrast to this, the multiple-cycle method calls for the re-routing of the gas flow around the EtOH for a short time period (3 min) before being re-routed back through the EtOH bubbler. This cycling was performed 3 times. The reason that a multiple-cycle method increased the CNT density is because the catalyst particles had more than one chance to become activated[35] in contrast with a single-cycle where the catalyst particles only have one chance to become activated. Using AFM characterization, the density of CNTs improved by 3-4 times when using the multiple-cycle method as compared to the single-cycle method. A single-cycle growth method produced ≈4 CNTs / 60 μm where a multiple-cycle method produces ≈15 CNTs / 60 μm. It should be noted that these densities were measured in close vicinity to the catalyst. The density of CNTs decreased as you moved further away from the catalyst. This decrease in density is advantageous for fabricating a carbon nanotube field effect transistor (CNFET).

Following the CVD synthesis, the nanotube diameters were characterized via AFM. Typically, the nanotube diameters were in the range of 1-2 nm. On occasion, the diameter would be slightly larger or smaller than 1-2 nm. An AFM image can be seen in Figure 13. The scale bar is 500 nm. The diameter of this CNT was determined to be 1.64 nm via a section analysis. The small dots in the image are thought to be catalyst particles that were not activated during CVD growth or possibly small deposits of amorphous carbon, which is sometimes formed during CNT synthesis.

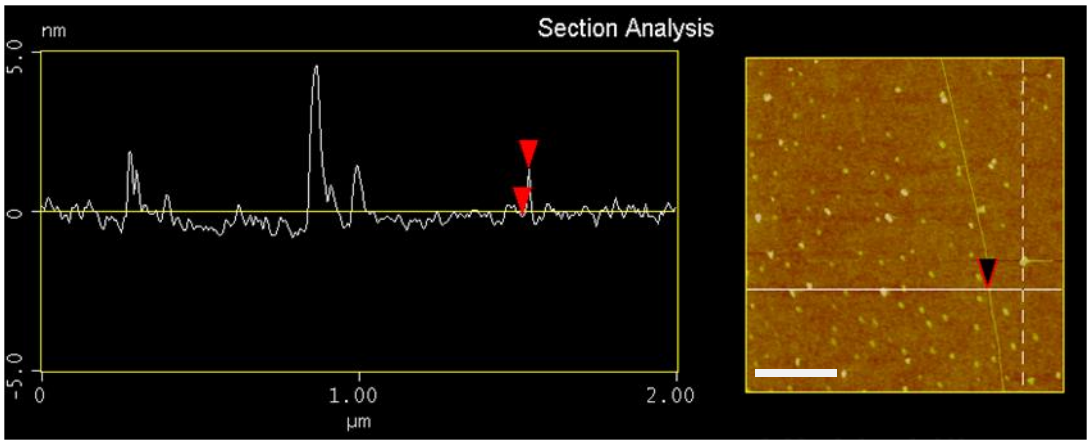

Figure 13. AFM image of a SWCNT collected prior to etching. The diameter was determined to be 1.64 nm. The small dots in the image are thought to be catalyst particles or possibly small deposits of amorphous carbon. The scale bar is 500 nm.

4.2 CNT CATALYZED ETCHING OF SILICON DIOXIDE

Following the CVD growth and diameter characterization of the CNTs, the samples were etched via a vapor-phase HF technique. Vapor-phase etching (VPE) was used rather than a solution-based etching because VPE allows for the CNTs to remain on the substrate after the etching process and it also has the capability to produce deeper trenches than a wet-etching process.

The etching of SiO_2 using HF vapor is thermodynamically favorable. The overall reaction can be seen in equation 5. The ΔG for this reaction @298K is -74.8 kJ/mol.[37]

$$SiO_2(s) + 4HF(g) \rightarrow SiF_4(g) + 2H_2O(g) \qquad (5)$$

In addition, it has been reported by Lee et al. that an alcohol such as MeOH can reduce the formation of solid residues on the etched surface and therefore improves etching characteristics such as roughness.[38]

Mechanistic studies have suggested that the etching is initiated by the deprotonation of HF by water (Equation 6). The products of Equation 6 then etch the SiO_2 surface via Equation 7.

$$6HF + 3H_2O \rightarrow 3HF_2^- + 3H_3O^+ \quad (6)$$

$$3HF_2^- + 3H_3O^+ + SiO_2 \rightarrow 2HF + SiF_4 + 5H_2O \quad (7)$$

Typically, the amount of water in the atmosphere is sufficient to initiate this etching process. As shown in Equation 7, water is also a product of the reaction. Hence, the reaction is autocatalytic.[39]

It has been shown by Allgair et al. that carbon can act as a catalyst for the etching of SiO_2.[40] Therefore, when a sample containing CNTs was exposed to the etching vapors, overtime a trench formed where a nanotube was in intimate contact with the SiO_2 surface. This area of the SiO_2 surface in close contact with a CNT etches at a different rate than bare SiO_2. Hence, overtime a trench is produced.

The goal of etching was to produce trenches that could be seen under an optical microscope which would allow for the location of an individual CNT to be precisely known. Etching parameters such as time and temperature were varied. It was found that temperatures

ranging from 70-100°C and times ranging from 30-70 minutes produced trenches that could be seen under an optical microscope. Typically, trench depths ranged from ≈10-30 nm, with the deepest trench being confirmed at 34 nm. Figure 14 is an AFM image of trenches in the SiO_2 surface. The trench indicated has a depth of 16.5 nm. The scale bar is 1 μm. The width of a trench typically ranged from 50-100 nm.

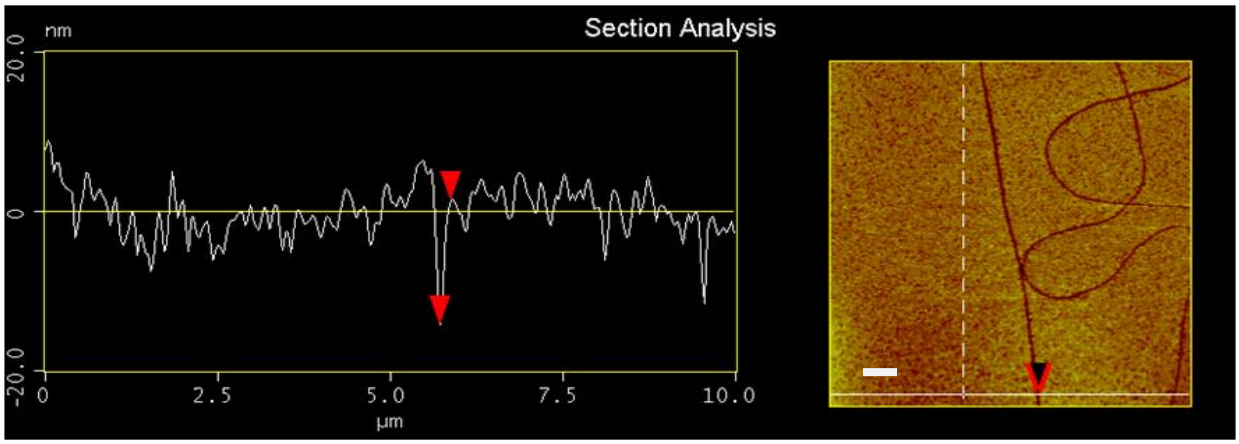

Figure 14. AFM image of trenches produced by the vapor-phase HF etching technique. The depth of the trench indicated is 16.5 nm as shown in the section analysis. The morphology of the trenches is typical of the morphology of the CNTs. The scale bar is 1 μm.

Following the optimization of the VPE method, the samples were examined under an optical microscope to observe for trenches on the substrate. An optical microscope image can be seen in Figure 15. The enclosed area indicates the area from which AFM images were collected to confirm that the structures observed were indeed trenches. An AFM mosaic was constructed and can be seen in Figure 16. The depths of these trenches were determined to range from 7.5 to 13.8 nm. The fact that trenches of this depth can be seen under an optical microscope can be

attributed to the interference properties of the SiO_2 thin film.[7] Note that the looping morphology of some of the trenches shown if Figure 15 is consistent with the morphology of the trenches in Figure 14. The white line towards the bottom of the figure is the catalyst line (Figure 15). The scale bar is 10μm.

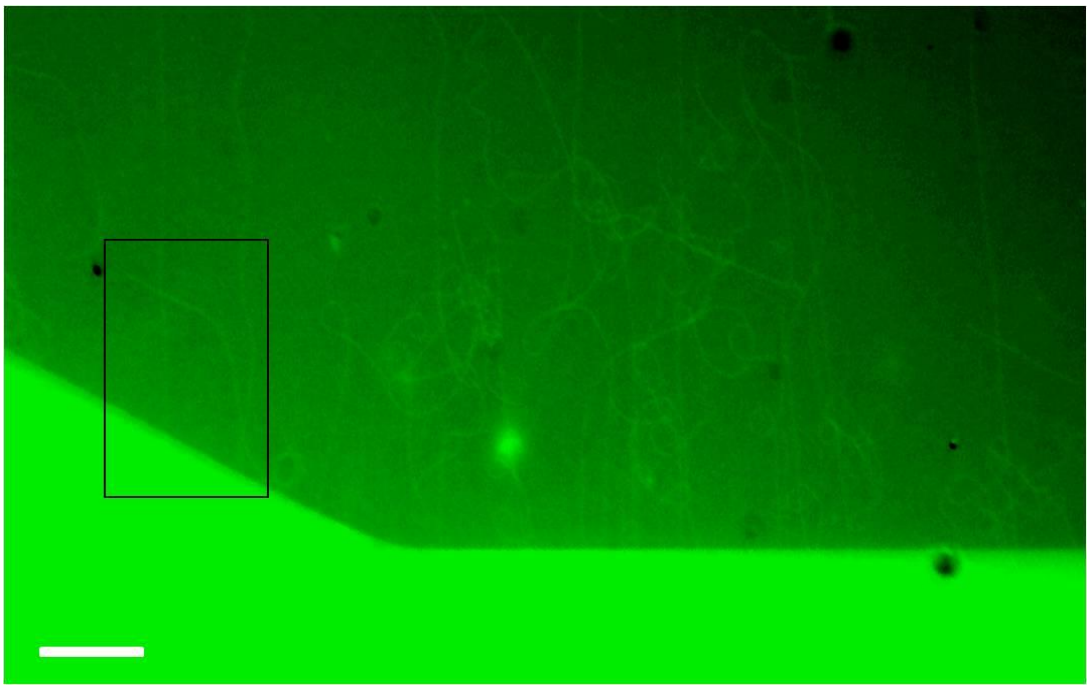

Figure 15. Optical microscope image of trenches produced by the VPE method. The image was collected with a 50x objective. Note the morphology of the various trenches and the catalyst line (white portion of image). The enclosed box indicates the area from which AFM images were taken to confirm that these structures were indeed trenches (see Figure 16). The scale bar is 10μm.

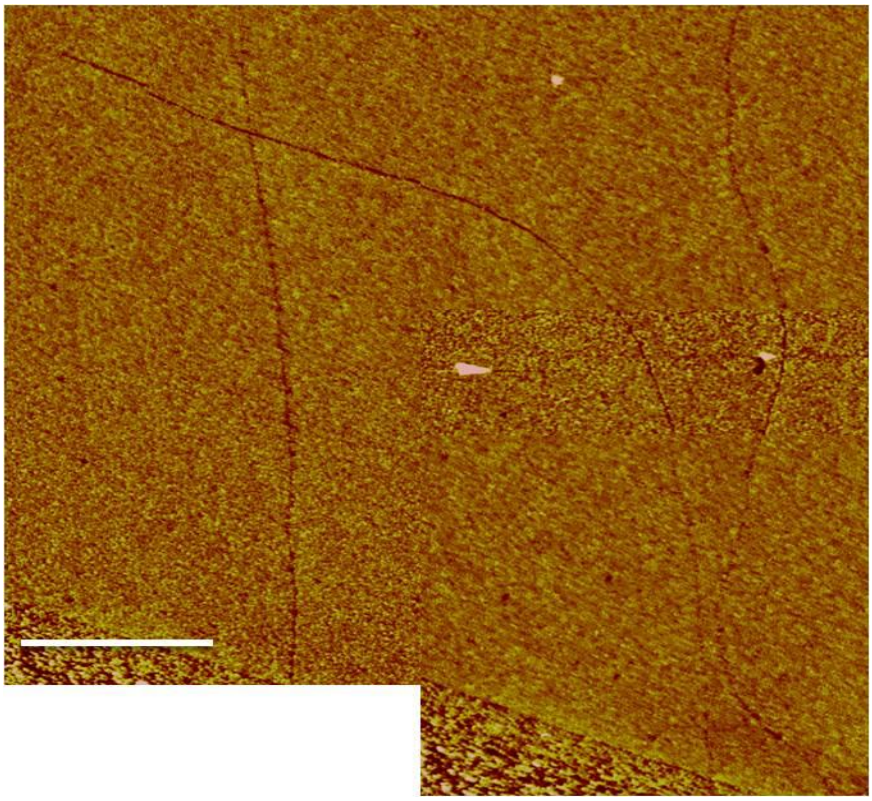

Figure 16. AFM mosaic collected from the enclosed area of Figure 15 confirming that the structures seen in the optical image are indeed trenches. The scale bar is 5 μm. Note the catalyst line running diagonally across the bottom of the figure. Trench depths range from 7.5 to 13.8 nm.

4.3 RAMAN SPECTRA COLLECTED FROM A TRENCH

To verify that the trenches observed in the optical images did in fact contain CNTs, Raman spectra were collected from various trenches. An optical image and the corresponding Raman spectrum are shown in Figure 17. The scale bar in the optical image (top) is 10μm and a 50x objective was used for its collection. The arrow in the optical image indicates the location that the spectrum (bottom) was collected. For this spectrum a 785nm (1.58 eV) laser was focused onto the trench and the integration time set to 600s. From its Raman spectrum, this CNT was

characterized as a semiconducting SWCNT after analysis of its G-band which is located at approximately 1590cm^{-1}. With use of Equation 4, its diameter was calculated to be 1.87 nm. Note the splitting of the G-band into the G^+ and G^- portions which is indicative of a SWCNT. The width of the G^- peak was used to determine that this CNT is semiconducting. The diameter and electronic assignment is supported by examination of the Kataura plot in Figure 11. Briefly, because a 1.58 eV laser was used to collect the Raman spectrum, a tube with $E_{ii} = 1.58 \pm 0.1$ eV should give a Raman signal. The intersection of two lines (in the Kataura plot) where $E_{ii} = 1.58$ eV and $d_t \approx 1.9$ nm, does fall on the edge of the S_{33} transition where S and the subscript 33 represent semiconducting and the 3-to-3 transition in the DOSs, respectively. Also, no apparent D-band is visible which shows that the nanotube is relatively free of defects and that the surface of the sample is mostly free of amorphous carbon.

Raman spectra were collected in the RBM and G' range for the CNT shown in Figure 17 but these peaks were not observed. Very few of the Raman spectra collected showed an RBM or G' band. This is thought to be due to the notion that possibly the trench itself is dampening the Raman signal. This idea is supported by observing Raman spectra that were collected from purchased CNTs that were drop-cast onto a Si/SiO_2 wafer. These wafers were not etched prior the collection of their Raman spectra. These spectra showed multiple RBM peaks hence it is thought that the trench is possibly dampening the RBM signal. Also, if the nanotubes being analyzed via Raman spectroscopy have a diameter larger than 2 nm, it is unlikely that their Raman spectra would show the RBM band.[30] In the case for the SWCNT who's spectrum is shown in Figure 17, its diameter was calculated to be 1.87 nm so the non-presence of an RBM band is thought to be due to trench-dampening of the RBM Raman signal.

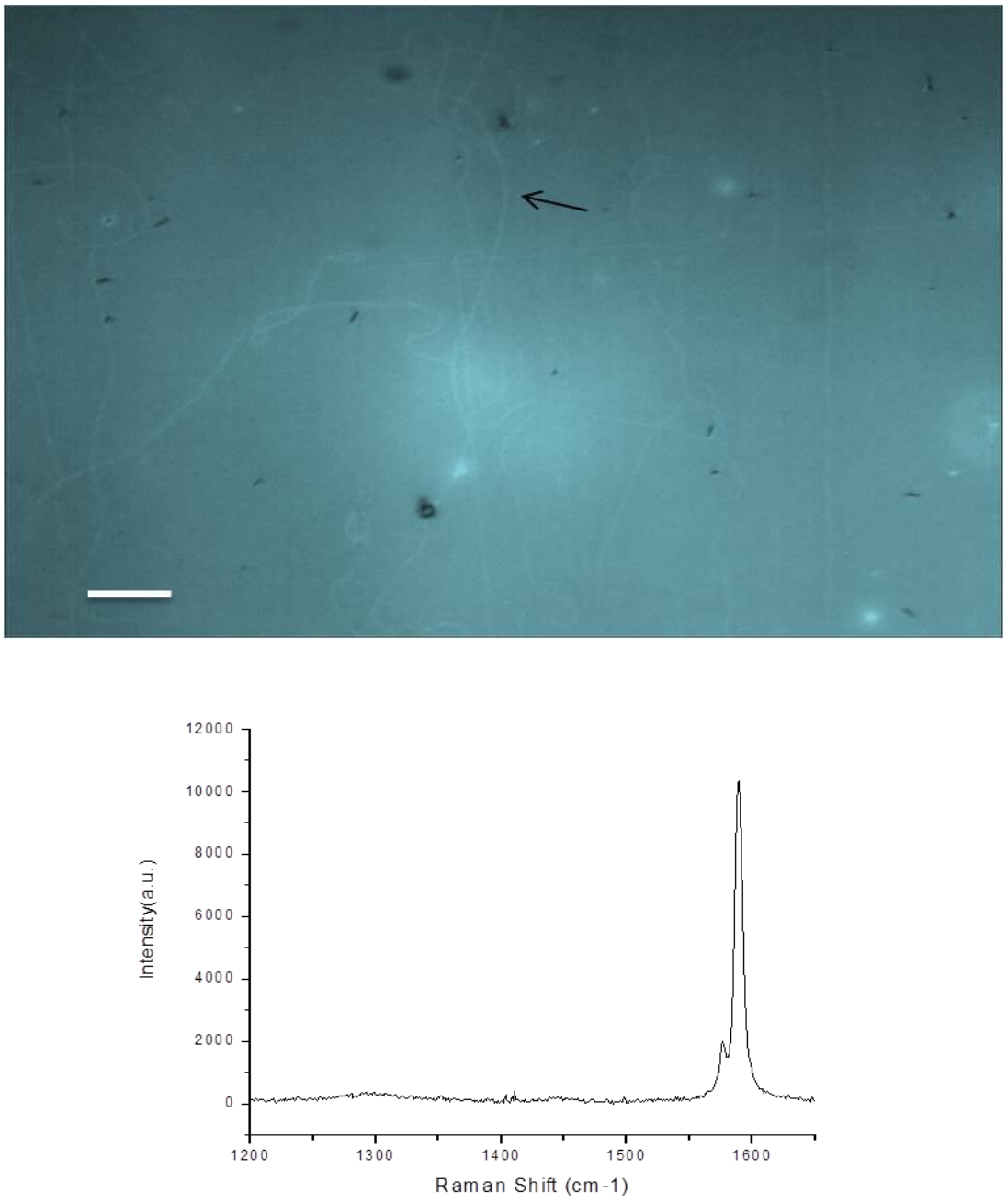

Figure 17. Optical image (top) of various trenches formed via VPE. The arrow indicates the spot where the laser was positioned for Raman collection. The scale bar is 10 μm. Raman spectrum (bottom) collected from the trench indicated in optical image.

4.4 UV-OZONE OXIDATION OF CARBON NANOTUBES

Upon confirming the presence of CNTs within the etched trenches, functionalization experiments were performed on the nanotube samples. The samples were treated with UV-ozone and their Raman spectra collected pre and post modification. This oxidation technique was chosen for modification because oxidation of a nanotube is typically the first step in a chemical functionalization scheme.[41] Ozone has been shown to chemisorb onto the nanotube, ultimately creating an epoxide or carbonyl. With increased exposure time, the carbon atoms that comprise the CNT are removed as CO or CO_2 and therefore the CNT is completely degraded after prolonged exposure to UV-O_3.[42] Overall, UV-O_3 is a route to controllably oxidize a CNT by monitoring exposure time. This method of oxidation is advantageous compared to other oxidation procedures (acid oxidation) because of shorter exposure/modification times and that it can be performed under ambient temperatures.

For the UV-O_3 oxidation experiments, a sample was irradiated with a mercury lamp in an oxygen atmosphere. This was performed at ambient pressure and temperature. Figure 18 shows the optical image of the sample (top) and the evolution of a CNTs Raman spectrum as a function of exposure time (bottom). The scale bar in the optical image is 10 μm. The arrow indicates the area from which the spectra were collected. The UV-O_3 exposure time is shown in the legend. All spectra were normalized using the Si overtone peak at ≈920 cm^{-1}. It should be noted that this is a different sample than that shown in Figure 17. The Raman spectra were collected with a 785 nm (1.58 eV) laser.

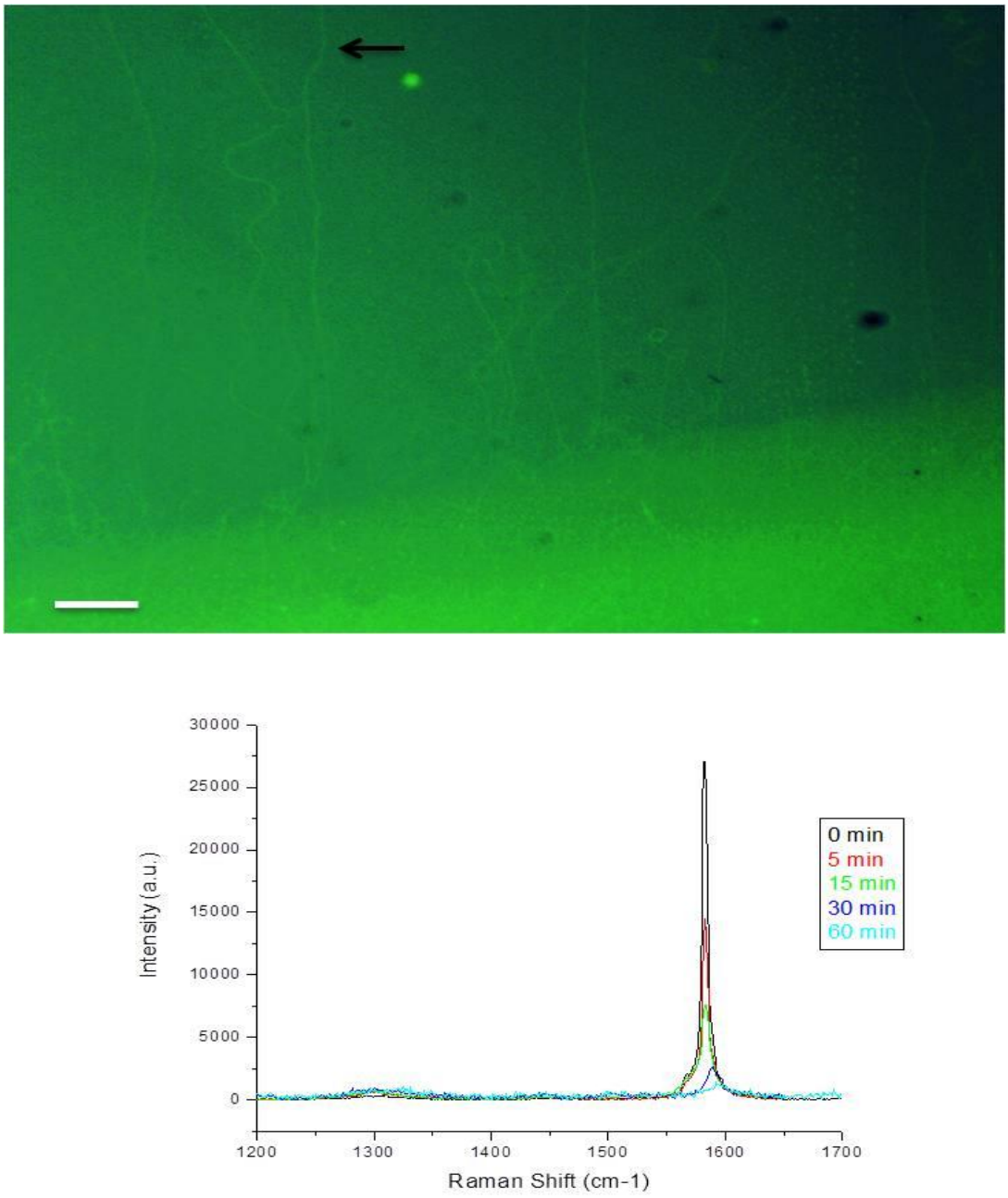

Figure 18. Optical image showing the location from which the spectra were collected. The scale bar is 10 µm (top). Raman spectra showing the evolution of a nanotube's D and G bands (bottom). All spectra were normalized using the Si overtone peak. The times represent total UV-O_3 exposure time.

The nanotube shown in Figure 18 was characterized to be a semiconducting SWCNT with a diameter of 1.75 nm (see Equation 4). Upon UV-O_3 exposure, initially there is a decrease in the G-band and an increase in the D-band. Even though the increase of the D-band is small, it is thought that this is due to the creation of defects in the CNT sidewall. A magnified image of the evolution of the D-band is shown in Figure 19. It can be seen that the largest increase in the D-band occurred after 5 minutes of exposure time. Upon further oxidation, the D-band intensity remained relatively constant.

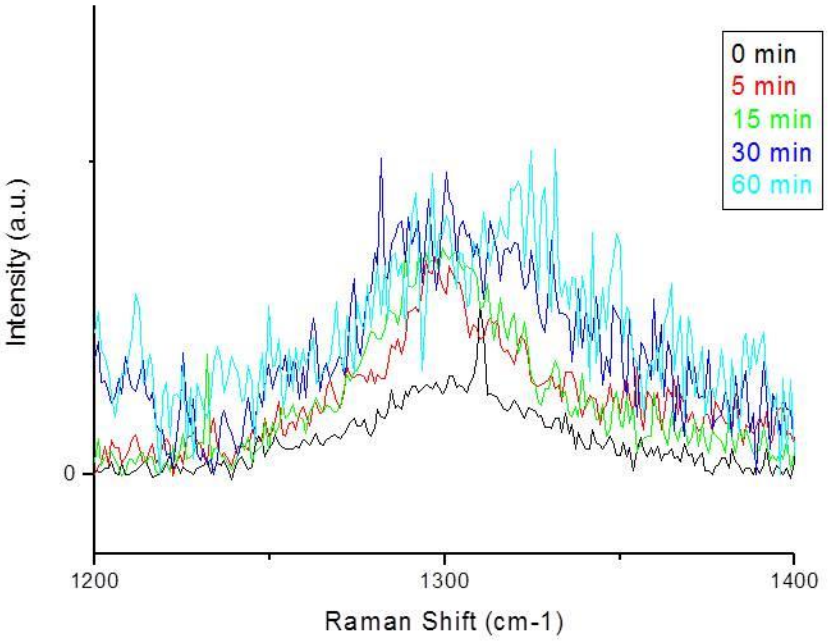

Figure 19. D-band region of the Raman spectrum shown in Figure 18. Note the evolution of the D-peak region upon UV-O_3 exposure.

The G-band had a much more dramatic change during UV-O_3 exposure. It steadily decreased upon prolonged exposure until it was barely observable in the Raman spectrum after 60 minutes of exposure time. This decrease can be attributed to the removal/destruction of the sp^2 carbon material. A shift in the G-band to higher frequencies was also observed. It is thought that this is due to the formation of amorphous carbon.[34]

A commonly used calculation to analyze defects in CNTs is the I_D/I_G ratio as shown in Figure 20. The peak area ratios were calculated using the spectra shown in Figure 18. Because the G-band intensity is assumed to be independent of defects, this ratio it typically used for defect evaluation.[43] The integrated peak areas were used to calculate the I_D/I_G ratio. The error bars represent the error associated the with the integrated peak area calculations. All peak area calculations were performed using OriginLab 6.1 Data Analysis and Graphing Software.

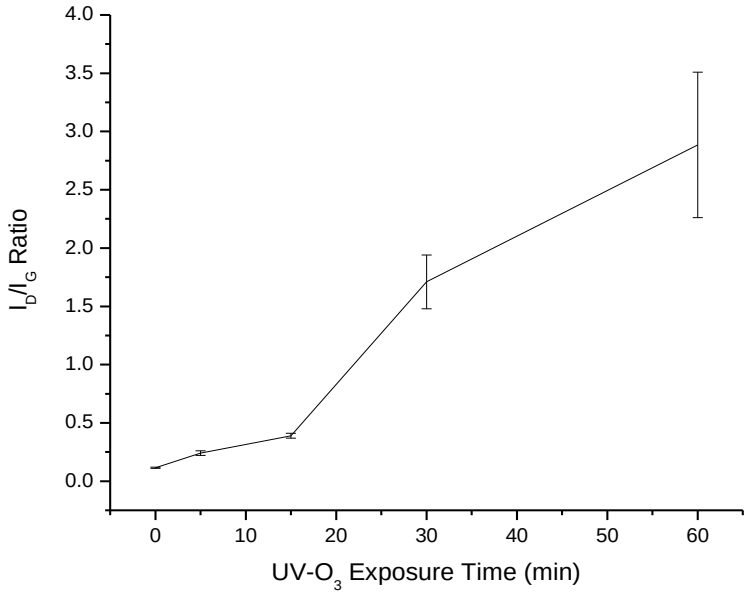

Figure 20. The I_D/I_G ratio from an individual SWCNT during UV-O3 exposure. This ratio was calculated by using the integrated peak areas from the Raman spectrum shown in Figure 18.

During the early stages of UV-O_3 exposure the ratio increased linearly with time. Simmons et al. have also reported a linear increase in the I_D/I_G ratio upon UV-O_3 exposure although their exposure time did not exceed 10 minutes.[34] It should be noted that they were analyzing CNT mats rather than individual CNTs. Monitoring the affects of UV-O_3 on an individual CNT demonstrates that the HF vapor-phase technique presented here does provide a route for the systematic analyses of CNTs.

5.0 CONCLUSIONS

5.1 SUMMARY

We have realized a high-throughput route for the optical visualization of a trench which contains an individual CNT. This allows for the precise location of an individual nanotube to be determined without the use of lithographic techniques or modification of the CNT. Knowing the precise location of an individual CNT is important because it allows for the systematic study of a given nanotube. The primary advantages of the VPE technique presented here are that it is less complex than other techniques and is also a very time-friendly approach. If implementing the VPE route described here, a CNT can be grown, the sample etched, its Raman spectrum collected, and the CNT modified all within a day's time.

The CNTs used in this project were synthesized via a Fe-catalyzed CVD method. The samples containing CNTs were then analyzed using AFM to determine the range of CNT diameters and also the CNT density. These samples were subsequently etched by the VPE method which was optimized, in regards to time and temperature, so that optically visible trenches could be consistently produced in the substrate. It was observed that trenches as shallow as 7-8 nm could be observed under an optical microscope. Raman spectroscopy was employed to verify that the trenches observed under the optical microscope did in fact contain CNTs.

Following confirmation of a CNT within a trench, a sample was then exposed to UV-O_3. The Raman spectrum of a given individual nanotube was collected pre and post modification. These spectra were collected from the same location on the nanotube of interest. It was shown that UV-O_3 exposure ultimately degraded the CNT. This was evident by a slight increase in its D-band intensity and a decrease in its G-band intensity. With prolonged exposure, the G-band decreased until it was almost unobservable. The I_D / I_G ratio was calculated and increased with increased exposure time. This increase was linear up to 15 minutes of exposure time. Beyond 15 minutes of exposure time, the ratio continued to increase but was not linear. This demonstrates that an individual nanotube within a trench can be rapidly and systematically analyzed when performing gas phase modifications on a CNT.

5.2 FUTURE DIRECTIONS

Presently, efforts are under way to create an FET based on an individual CNT. Because a CNTs location can be precisely known, it is thought that metal contacts can be manually applied to a trench, which is visible under an optical microscope. Therefore, the VPE method presented here may provide a high-throughput route for CNFET fabrication based on an individual CNT. The efforts made in creating a CNFET have been unsuccessful thus far. Devices have been fabricated but there has been no observable current to this point. A possible explanation for this is that the Ag metal particles used for contacts are too large and cannot reach the bottom of the trench to make contact with the CNT. To confirm this idea, a cross-section SEM image of the sample could be collected. If the SEM image would show that the Ag particles cannot reach the bottom of the trench to make contact with the CNT, metal evaporation techniques could be implemented

but it is ultimately hoped that the more simplistic manual application route is possible rather than metal evaporation.

Another topic of interest in the fields of materials chemistry and engineering is to have the capability to manually move an individual CNT. It is thought that this could be done by applying an epoxy or glue to a trench which contains a nanotube. Due to the fact that the trench is optically visible, one would know exactly where to apply the epoxy/glue. Another, slightly more complex method to physically move a CNT could be to attach magnetic nanoparticles to the CNT sidewalls. A magnet could then be used to physically move the CNT to a desired location. To confirm that the CNT has been moved, by either method, a Raman spectrum could be collected from a trench to confirm that it does contain an individual nanotube, the epoxy/glue or nanoparticles applied and the CNT removed. A second Raman spectrum could be collected from the same trench to observe for a CNT Raman signal. Having the ability to manually move a CNT to a desired location would be of great interest because this could potentially pave the way for creating various types of CNT structures with varying architectures.

BIBLIOGRAPHY

1. Iijima, S. Helical Microtubules of Graphitic Carbon. *Nature*. **1991**, 354, 56-58
2. Baughman, R.H.; Zakhidov, Anvar A.; de Heer, Walt A. Carbon Nanotubes-The Route Toward Applications. *Science*. **2002**, 297, 787-792
3. Villalpando-Paez, F.; Son, H.; Nezich, D.; Hsieh, Y.P.; Kong, J.; Kim, Y.A.; Shimamoto, D.; Maramatsu, H.; Hayashi, T.; Endo, M.; Terrones, M; Dresselhaus, M.S. Raman spectroscopy study of Isolated Double-Walled Carbon Nanotubes With Different Metallic and Semiconducting Configurations. *Nano Letters*. **2008**, 8, 3879-3886
4. Zhang, Rufan; Zhang, Yingying; Zhang, Qiang; Xie, Huanhuan; Wang, Haidong; Nie, Jingqi; Wen, Qian; Wei, Fei. Optical Visualization of Individual Ultralong Carbon Nanotubes by Chemical Vapour Deposition of Titanium Dioxide Nanoparticles. *Nature Communications*. **2013**,4:1727
5. Chen, Yi-Chieh; Young, Robert J.; Macpherson, Julie V.; Wilson, Neil R. Single-Walled Carbon Nanotube Networks Decorated with Silver Nanoparticles: A Novel Graded SERS Substrate. *J. Phys. Chem. C*. **2007**, 111, 16167-16173
6. Chu, Haibin; Wang, Jinyong; Ding, Lei; Yuan, Dongning; Zhang, Yan; Liu, Jie; Li, Yan. Decoration of Gold Nanoparticles on Surface-Grown Single-Walled Carbon Nanotubes for Detection of Every Nanotube by Surface-Enhanced Raman Spectroscopy. *J. Am. Chem. Soc.* **2009**, 131, 14310-14316
7. Hiep, Ha Minh; Yoshikawa, Hiroyuki; Saito, Masato; Tamiya, Eiichi. An Interference Localized Surface Plasmon Resonance Biosensor Based on the Photonic Structure of Au Nanoparticles and SiO_2/Si Multilayers. *ACS Nano*. **2009**, 3, 446-452
8. Liu, Haito; Steigerwald, Michael L.; Nuckolls, Colin. Electrical Double Layer Catalyzed Wet-Etching of Silicon Dioxide. *J. Am. Chem. Soc.* **2009**, 131, 17034-17035
9. Avouris, Phaedon; Appenzeller, Joerg. Electronics and Optoelectronics with Carbon Nanotubes. *The Industrial Physicist*. **2004**, 18-21
10. Castro Neto, Antonio H. The Carbon New Age. *Materials Today*. **2010**, 13, 1-6
11. Dresselhuas, M.S.; Dresselhaus, G.; Eklund, P.C. *Science of Fullerenes and Carbon Nanotubes*, Academic Press, 1996, pp 437-438
12. Dresselhaus, M.S.; Dresselhaus, G.; Saito, R.; Jorio, A. Raman Spectroscopy of Carbon Nanotubes. *Physics Reports*. **2004**, 4-5

13. Dresselhuas, M.S.; Dresselhaus, G.; Jorio, A.; Filho, A. G. Souza; Pimenta, M.A.; Saito, R. Single Nanotube Spectroscopy. *Accounts of Chemical Research*. **2002**, 35, 1070-1078
14. Fox, Mark. *Optical Properties of Solids, 2nd* ed.; Oxford University Press. 2010; pg 143
15. Samsonidze, Ge.G.; Saito, R.; Jorio, A.; Pimenta, M.A.; Filho, A.G. Souza; Gruneis, A.; Dresselhaus, G.; Dresselhaus, M.S. The Concept of Cutting Lines in Carbon Nanotube Science. *Journal of Nanoscience and Nanotechnology*. **2003**, 3, 431-458
16. Ihn, Thomas. *Semiconductor Nanostructures*. Oxford University Press. 2010; pg 27
17. Kumar, Mukul; Ando, Yoshinori. Chemical Vapor Deposition of Carbon Nanotubes: A Review on Growth Mechanism and Mass Production. *Journal of Nanoscience and Technology*. **2010**, 10, 3739-3758
18. Szabo, Andrea; Perri, Caterina; Csato, Anita; Giordano, Girolamo; Vuono, Danilo; Nagy, Janos B. Synthesis Methods of Carbon Nanotubes and Related Materials. *Materials*. **2010**, 3, 3092-3140
19. Prasek, Jan; Drbohlavova, Jana; Chomoucka, Jana; Hubalek, Jaromir; Jasek, Ondrej; Adam, Vojtech; Kizek, Rene. Methods for Carbon Nanotube Synthesis Review. *Journal of Materials Chemistry*. **2011**, 21, 15872-15884
20. Cao, Guozhong; Wang, Ying. *Nanostructures and Nanomaterials*, 2nd ed.; World Scientific, 2011; pp 301-307
21. Horvath, Z.E.; Kertesz, K.; Petho, L.; Koos, A.A.; Tapaszto, L.; Vertesy, Z.; Osvath, Z.; Darabont, Al.; Nemes-Incze, P.; Sarkozi, Zs.; Biro, L.P. Inexpensive Upscale Nanotube Growth Methods. *Current Applied Physics*. **2006**, 6, 135-140
22. Raty, Jean-Yves; Gygi, Francios; Galli, Giulia. Growth of Carbon Nanotubes on Metal Nanoparticles: A Microscopic Mechanism from Ab Initio Molecular Dynamics Simulations. *Physical Review Letters*. **2005**, 95, 096103
23. Fahlman, Bradley F. *Materials Chemistry*; Springer Science, 2008, pp 319-341
24. Hornyak, Gabor L.; Dutta, Joydeep; Tibbals, Harry F.; Rao, Anil K. *Introduction to Nanoscience*; CRC Press, 2008, 142-154
25. Wilson, Neil R.; Macpherson, Julie V.; Carbon Nanotubes Tips for Atomic Force Microscopy. *Nature Nanotechnology*. **2009**, 4, 483-491
26. Jorio, A.; Saito, R.; Hafner, J.H.; Lieber, C.M.; Hunter, M.; McClure, T.; Dresselhaus, G.; Dresselhaus, M.S. Structural (n,m) Determination of Isolated Single-Wall Carbon Nanotubes by Resonant Raman Scattering. *Physical Review Letters*. **2001**, 86, 1118-1121
27. Ball, David W. *Physical Chemistry*; Brooks and Cole, 2003, pp 511-514
28. Harris, Daniel C.; Bertolucci, Michael D. *Symmetry and Spectroscopy: An Introduction to Vibrational and Electronic Spectroscopy*; Oxford University Press, 1978, pp 93-98
29. Dresselhaus, M.S.; Dresselhaus, G.; Jorio, A.; Filho, A.G. Souza; Saito, R. Raman Spectroscopy on Isolated Single Wall Carbon Nanotubes. *Carbon*. **2002**, 40, 2043-2061
30. Jorio, A.; Pimenta, M.A.; Filho, A.G. Souza; Saito, R.; Dresselhaus, G.; Dresselhaus, M.S. Characterizing Carbon Nanotube Samples with Resonance Raman Scattering. *New Journal of Physics*. **2003**, 5, 139.1-139.17

31. Filho, A.G. Souza; Jorio, A.; Hafner, J.H.; Lieber, C.M.; Saito, R.; Pimenta, M.A.; Dresselhaus, G.; Dresselhaus, M.S. Electronic Transition Energy E_{ii} for an Isolated (n,m) Single-Wall Carbon Nanotube Obtained by Anti-Stokes/Stokes Resonant Raman Intensity Ratio. *Physical Review B*. **2001**, 63, 241404
32. Liu, Jie; Dossot, Manual; Olevik, David; Mamane, Victor; Vigolo, Brigitte; Abrahamsson, David; Jonsson, Henrik; Fort, Yves; Humbert, Bernard; Soldatov, Alexander V.; McRae, Edward. Preferential Functionalisation of Carbon Nanotubes Probed by Raman Spectroscopy. *Physica E*. **2008**, 40, 2343-2346
33. Jorio, A.; Filho, A.G. Souza; Dresselhaus, G.; Dresselhaus, M.S.; Swan, A.K.; Unlu, M.S.; Goldberg, B.B.; Pimenta, M.A.; Hafner, J.H.; Lieber, C.M.; Saito, R. G-Band Resonant Raman Study of 62 Isolated Single Wall Carbon Nanotubes. *Physical Review B*. **2002**, 65, 155412
34. Simmons, J.M.; Nichols, B.M.; Baker, S.E.; Marcus, Matthew S.; Castellini, O.M.; Lee, C.S.; Hamers, R.J.; Eriksson, M.A. Effect of Ozone Oxidation on Single-Walled Carbon Nanotubes. *Journal of Physical Chemistry B*. **2006**, 110, 7113-7118
35. Zhou, Weiwei; Ding, Lei; Yang, Sungwoo; Liu, Jie. Synthesis of High-Density, Large-Diameter, and Aligned Single-Walled Carbon Nanotubes by Multiple-Cycle Growth Methods. *ACS Nano*. **2011**, 5, 3849-3857
36. Zheng, L.X.; O'Connell, M.J.; Doorn, S.K.; Liao, X.Z.; Zhao, Y.H.; Akhadov, E.A.; Hoffbauer, M.A.; Roop, B.J.; Jia, Q.X.; Dye, R.C.; Peterson, D.E.; Huang, S.M.; Liu, J.; Zhu, Y.T. Ultralong Single-Wall Carbon Nanotubes. *Nature Materials*. **2004**, 3, 673-676
37. Butterbaugh, J.W.; Muscat, A.J. *Handbook of Silicon Wafer Cleaning Technology*. 2nd ed.; William Andrew Inc., 2008, pp 269-353
38. Lee, Yong-ll; Park, Kyung-Ho; Lee, Jonghyun; Lee, Chen-Su; Yoo, Hyung J.; Kim, Chang-Jin; Yoon, Yong-San. Dry Release for Surface Micromachining With HF Vapor-Phase Etching. *Journal of Microelectromechanical Systems*. **1997**, 6, 226-233
39. Surwade, Sumedh P.; Zhao, Shichao; Liu, Haito. Molecular Lithography Through DNA-Mediated Etching and Masking of SiO_2. *Journal of the American Chemical Society*. **2011**, 133, 11868-11871
40. Allgair, J.; Ryan, J.M.; Song, H.J.; Kozicki, M.N.; Whidden, T.K.; Ferry, D.K. Nanoscale Patterning of Silicon Dioxide Thin Films by Catalyzed HF Vapor Etching. *Nanotechnology*. **1996**, 7, 351-355
41. Hussain, S.; Jha, P.; Chouksey, A.; Raman, R.; Islam, S.S.; Islam, T.; Choudhary, P.K.; Harsh. Spectroscopic Investigation of Modified Single Wall Carbon Nanotube. *Journal of Modern Physics*. **2011**, 2, 538-543
42. Larciprete, Rosanna; Fabris, Stefano; Sun, Tao; Lacovig, Paolo; Baraldi, Allesandro; Lizzit, Silvano. Dual Path Mechanism in the Thermal Reduction of Graphene Oxide. *Journal of the American Chemical Society*. **2011**, 133, 17315-17321

43. Kalbac, Martin; Hsieh, Ya-Ping; Farhat, Hootan; Kavan, Ladislav; Hoffmann, Mario; Kong, Jing; Dresselhaus, Mildred S. Defects in Individual Semiconducting Single Wall Carbon Nanotubes: Raman Spectroscopic and in Situ Raman Spectroelectrochemical Study. *Nano Letters*. **2010**, 10, 4619-4626